Chapter 6

Testing the Stochastic Flow Rule[1]

6.1 Introduction

In chapters 3 and 4 it was shown that the spot model simulation could reproduce many features of granular drainage to a high degree of accuracy. However, a key drawback is that it appears difficult to generalize to other forms of granular flow. While the concept of a local relaxation appears general, the concept of a diffusing free volume appears to be very specific to granular drainage, where one can make an easy identification with particles exiting, and free volume being injected. In other situations, such as a shear cell, or plate dragging, the motion of free volume appears a lot less clear.

It also seems difficult to generalize the specific random walk process that was used. While the approximately-gaussian velocity profiles in granular drainage, or the error function profiles seen in shear zone experiments [45] seem to warrant explanation by a diffusing object, other types of granular flows show different functional forms which are less associated with diffusion. In Couette cell experiments, velocity profiles have been shown to be exponential, while on inclined planes the velocity profiles show a polynomial dependence, and it appears more difficult to explain these quantities in terms of a diffusing object. Even in granular drainage, the results of the previ-

[1]This chapter is based on reference [66], *The Stochastic Flow Rule: A Multi-Scale Model for Granular Plasticity*, published in Modelling and Simulation in Materials Science and Engineering, 2007. See `http://www.iop.org/journals/msmse/` for more details.

ous two chapters suggest that the spot model random walk process may be a large oversimplification.

One of the attractions of the spot model for granular drainage is its motivation from mainly geometrical reasoning. However, it seems that a general model for granular flow must ultimately be grounded in mechanical concepts. Formulating a mechanical model for dense granular flow has an extremely long history, dating back to Coulomb, who proposed the "Ideal Coulomb Material": an idealized infinitesimal element of material that would fail under certain stress conditions. Using this microscopic picture, Mohr-Coulomb plasticity theory was developed [94, 118]. This theory has become widely-accepted, but cannot be considered at a complete theory of granular materials, since it fails to provide an accurate prediction of many granular flows, and it is also numerically ill-posed, sometimes leading to shocks – this is discussed in more detail in the following section.

While physical ideas should play a role in a general theory, the results of the previous sections suggest that particle discreteness plays an integral role in granular flow. Perhaps Mohr-Coulomb plasticity's largest failure is that it assumes a continuum throughout. Based on these ideas, Kamrin and Bazant formulated the Stochastic Flow Rule (SFR) [65], attempting to rectify traditional plasticity theories by accounting for the particle discreteness. The SFR provides a physical basis for the spot model simulations considered in previous chapters, and predicts several of the free parameters that were originally calibrated in chapter 3. In addition, it also correctly predicts the exponential flow profile seen in the annular Couette cell, and at the time of writing, we are not aware of any other model, continuum or discrete, which can describe both of these cases, even qualitatively.

In this chapter, the continuum predictions of the SFR are tested. In section 6.4 the velocity profiles for a wide silo and an annular Couette cell are computed, and in section 6.5 these are directly compared with DEM simulations in these two geometries.

6.2 Continuum theories for two dimensional stress

Coulomb proposed the "Ideal Coulomb Element" as a representation of two dimensional infinitesimal element of a dry cohesionless granular material. The element is subject to a shear stress τ and a normal stress σ. The material is rigid (perfectly plastic) until failure occurs when

$$|\tau/\sigma| > \mu, \tag{6.1}$$

where μ is an internal friction coefficient which is a constant for the material. It is also convenient to define a friction angle $\phi = \tan^{-1}\mu$.

From this microscopic picture of an element, we would like to form a continuum model, by using momentum balance. However, to get a closed system of equations, additional assumptions are needed. An obvious problem stems from equation 6.1 being an inequality, corresponding to the fact granular materials have a memory, and may have internal state variables that were set by their method of preparation.

To make progress, we consider the Critical State Theory of soils [118]. In this theory, the stresses in a soil during flow converge on a "critical state line" in which the pressure and the deviatoric stress tensor $\mathbf{D_0} = \mathbf{D} - \mathbf{I}(\operatorname{tr}\mathbf{D})/3$ are linearly related. This Drucker-Prager yield criterion is similar to the three dimensional analog of the Mohr-Coulomb yield function. Thus, if we wish to compute stresses in a flowing environment, we assume the *Mohr-Coulomb incipient yield hypothesis*, that $|\tau/\sigma| = \mu$ everywhere.

Let us focus entirely on 2D geometries (plane strain) complete with a 2D stress tensor $\mathbf{T}$ defined in the plane of the flow. By requiring the yield criterion to be met at all points, the limit-state assumption implies the following constraint: $\frac{1}{\sqrt{2}}|\mathbf{T}_0| = \sin\phi\left(\frac{1}{2}\operatorname{tr}\mathbf{T}\right)$, where $\mathbf{T}_0$ is the deviatoric stress tensor and $|\mathbf{A}| = \sqrt{\mathbf{A}:\mathbf{A}}$. A simple way to uphold this constraint is to rewrite the stress field in terms of two stress parameters (the Sokolovskii variables [127]): the average pressure p, and the "stress-angle" ψ denoting the angle from the horizontal to the major principal stress. The

components of the 2D stress tensor are then

$$\begin{aligned} T_{xx} &= -p(1+\sin\phi\cos 2\psi) && (6.2)\\ T_{yy} &= -p(1-\sin\phi\cos 2\psi), && (6.3)\\ T_{xy}=T_{yx} &= -p\sin\phi\sin 2\psi && (6.4) \end{aligned}$$

from which it can be seen that $p = -\operatorname{tr}\mathbf{T}/2$ and $\tan 2\psi = 2T_{12}/(T_{11}-T_{22})$. The convection-free 2D momentum balance law $\boldsymbol{\nabla}\cdot\mathbf{T}+\mathbf{F}_{\text{body}}=\mathbf{0}$ then reduces to the two variable system of hyperbolic PDEs

$$\begin{aligned} F^x_{\text{body}} &= (1+\sin\phi\cos 2\psi)p_x - 2p\sin\phi\sin 2\psi\ \psi_x \\ &\quad +\sin\phi\sin 2\psi\ p_y + 2p\sin\phi\cos 2\psi\ \psi_y && (6.5)\\ F^y_{\text{body}} &= \sin\phi\sin 2\psi\ p_x + 2p\sin\phi\cos 2\psi\ \psi_x \\ &\quad +(1-\sin\phi\cos 2\psi)p_y + 2p\sin\phi\sin 2\psi\ \psi_y. && (6.6) \end{aligned}$$

The directions along which the yield criterion is met, the slip-lines, form at the angles $\psi\pm\epsilon$ from the horizontal where $\epsilon=\pi/4-\phi/2$.

To compute a velocity field, we need to specify a flow rule, which relates the deformation rate tensor $\mathbf{D}$ to the stress tensor, specifying how the material will flow during failure. A common assumption here is *coaxiality* which assumes that the eigenvectors of $\mathbf{T}$ and $\mathbf{D}$ are aligned. This assumption comes from a belief that the material is isotropic (even at the local scale), and thus if the material is pushed on a certain set of axes, the response will also be aligned with those axes. In this situation, it says that when a material element fails, it fails equally along both slip lines at the same time.

Unfortunately, the resulting system of equations for $\mathbf{T}$ is extremely difficult to solve. In many situations, and even in some simple geometries, the equations predict shocks [94], which require sophisticated mathematical techniques to solve [52, 53, 54]. Given the large debate about forces in granular packings at the microscopic level, the presence of shocks in this theory may not be fatal, and perhaps these shocks

characterize a physical concept, such as particle arching. However, what is perhaps more troubling is that with the assumption of a coaxial flow rule, these theories would predict discontinuities in the flow field also, and from all experiments and simulations considered in this thesis, granular flows have always exhibited smooth flow fields.

6.3 The Stochastic Flow Rule

The Stochastic Flow Rule proposed by Kamrin and Bazant [65, 66] attempts to resolve the above problems by assuming continuum stresses, but proposing that the flow made up of the superposition of many discrete plastic flow events. They remove the assumption of coaxiality, suggesting that it does not make sense for a discrete chunk of granular material to deform along both slip planes. Instead, they suggest that at each instant, the material will pick one slip plane randomly. Motivated by geometrical considerations, they suggest that the size for these plastic deformation events happens on the scale of spot.

Thus, they postulate that to generalize the spot model to an arbitrary geometry, one can first calculate the Mohr-Coulomb stresses, and then generate flow by imagining that spots carry out random walks on the lattice of Mohr-Coulomb slip lines. Since the flow is generated by the spots which are a diffusing quantity, the predicted flow field will be much smoother than that predicted by Mohr-Coulomb plasticity, with discontinuities blurred out by diffusion.

To model this mathematically, they assume that the spot concentration follows a Fokker-Planck equation

$$\frac{\partial \rho_s}{\partial t} + \boldsymbol{\nabla} \cdot (\mathbf{D}_1 \rho_s) = (\boldsymbol{\nabla} \otimes \boldsymbol{\nabla}) : (\mathbf{D}_2 \rho_s). \tag{6.7}$$

In steady-state flow, this simplifies to the time-independent drift-diffusion equation,

$$\boldsymbol{\nabla} \cdot (\mathbf{D}_1 \rho_s) = (\boldsymbol{\nabla} \otimes \boldsymbol{\nabla}) : (\mathbf{D}_2 \rho_s) \tag{6.8}$$

where $\mathbf{A} : \mathbf{B} = A_{ij} B_{ij}$. Once solved, the mean particle velocity field $\mathbf{u}$ can be found

by superposing the effects of all spots on all the particles. As discussed in previous chapters, this can be calculated by convolving the spot influence function $w(\mathbf{r}, \mathbf{r}')$ with the negative spot flux vector

$$\mathbf{u}^* = -\mathbf{D}_1\rho_s + \boldsymbol{\nabla} \cdot (\mathbf{D}_2\rho_s). \tag{6.9}$$

Thus the particle velocity $\mathbf{u}$ is

$$\mathbf{u} = \int w(\mathbf{r}, \mathbf{r}')\mathbf{u}^*(\mathbf{r}')d\mathbf{r}'. \tag{6.10}$$

The influence function, which in simple language describes the spot's shape, should have a characteristic width of three to five particle diameters, so that spots match known correlation length data. In many situations, $\mathbf{u}^*$ is close to $\mathbf{u}$ since the convolution with w tends only to smooth out sharp changes in the spot flux density.

The remaining question is to derive the spot drift $\mathbf{D}_1$ and diffusion $\mathbf{D}_2$ from mechanical principles from the underlying stress field. To begin, several assumptions are made, such as proposing that the diffusion is isotropic so that $\mathbf{D}_2 = D_2\mathbf{I}$, and that all length scales are set to the spot length scale, so that $|\mathbf{D}_1| = L_s/\Delta t$, and $D_2 = L_s^2/2\Delta t$. All that remains is to find the direction of the spot drift, which can be calculated from looking at local stress imbalances; for a full treatment, the reader should refer to [65] and [66].

6.4 Solutions for the flow in two simple geometries

6.4.1 Wide silo

For the wide, 2D silo with smooth walls and a flat bottom, the stress balance equations can be solved analytically, giving

$$\psi = \frac{\pi}{2}, \qquad p = \frac{f_g(z_m - z)}{1 + \sin\phi} \tag{6.11}$$

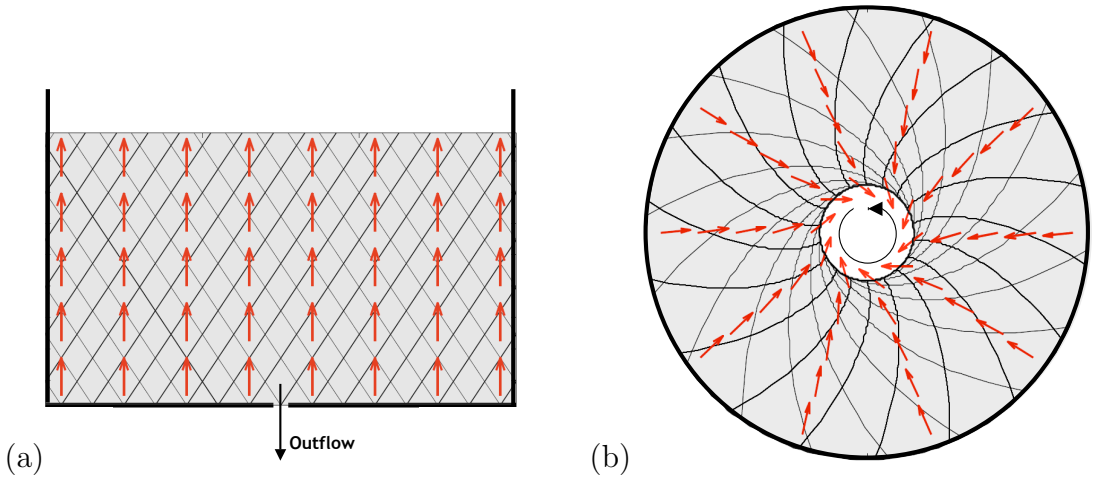

Figure 6-1: Slip-line fields (from Mohr-Coulomb Plasticity) and the spot drift field (from the SFR) displayed for (a) a wide silo draining under gravity, and (b) shearing in an annular Couette cell (no gravity).

where z is the distance from the silo bottom, z_m is the distance from the bottom to the free surface, and f_g is the material's weight density. As described in [66] this results in a regular lattice of diagonal slip lines, with a spot drift vector pointing uniformly upwards. Thus, we recover a spot density which satisfies a diffusion equation

$$\frac{\partial \rho_s}{\partial z} = \frac{L_s}{2} \boldsymbol{\nabla}^2 \rho_s. \tag{6.12}$$

as in the formulation in the previous chapters, and for a point orifice we obtain

$$\rho_s \approx \frac{\exp(-x^2/4bz)}{\sqrt{4\pi bz}} \tag{6.13}$$

where the diffusion parameter is given by $b = L_s/2$. This matches the previous analysis, but here the diffusion parameter no longer needs to be fitted; it is given directly by the spot length. Using the typical range of spot lengths to be $3d < L_s < 5d$, the typical range of b values is predicted to be $1.5d$ to $2.5d$, which compares very well to the results of previous chapters. In the literature [95, 114, 27, 137, 84], granular drainage experiments have predicted a range for b between $1.3d$ and $3.5d$, in good agreement with the prediction.

6.4.2 Annular Couette cell

In annular Couette flow, material fills the region between two rough cylinders and is sheared by rotating the inner cylinder while holding the outer stationary. To solve for the stresses, we first convert the stress balance equations to polar coordinates (r, θ) and require that p and ψ obey radial symmetry. This simplifies to

$$\frac{\partial \psi^*}{\partial r} = -\frac{\sin 2\psi^*}{r(\cos 2\psi^* + \sin \phi)}, \qquad \frac{\partial \eta}{\partial r} = -\frac{2 \sin \phi}{r(\cos 2\psi^* + \sin \phi)} \tag{6.14}$$

where $\eta = \log p$ and $\psi^* = \psi + \frac{\pi}{2} - \theta$. As described in [66], this must be solved numerically using fully rough inner wall boundary conditions. As shown in figure 6-1 this gives a drift field that points inward, but gradually opposes the motion of the inner wall. The competition between diffusion, and an inwards-point diffusion leads to an approximately exponential velocity profile.

To find the velocity field $\mathbf{u}$ requires convolving the solution for spot drift $\mathbf{u}^*$ with the spot influence function. To obtain a solution close to the walls requires a specification of how spots interact with the wall, and we consider two separate hypotheses:

1. Assume the $\mathbf{u}^*$ equals the wall velocity wherever spots overlap with the wall.

2. View the region inside the wall as a bath of non-diffusive spots which cause particles to move in a manner which mimics the rigid wall motion.

The second hypothesis creates velocity profiles which decay faster. Regardless of which hypothesis is chosen, the bulk behavior remains the same.

6.5 Comparing SFR Predictions to DEM Simulations

6.5.1 The silo geometry

We considered DEM simulations of a quasi-2D silo with plane walls at $x = \pm 75d, z = 0$ with friction coefficient $\mu_w = 0.5$, and made the y direction periodic with width $8d$. To generate an initial packing, 90,000 spherical particles with contact friction coefficient $\mu_c = 0.5$ were poured in from a height of $z = 130d$ at a rate of $378\tau^{-1}$. After all particles are poured in at $t = 238\tau$, the simulation is run for an additional 112τ in order for the particles to settle. After this process has taken place, the particles in the silo come to a height of approximately $z = 62.2d$. To initiate drainage, an orifice in the base of the container is opened up over the range $-3d < x < 3d$, and the particles are allowed to fall out under gravity; figure 6-2 shows a typical simulation snapshot during drainage.

We collected 282 snapshots every 2τ, and made use of this information to construct velocity cross sections. A particle with coordinates $\mathbf{x}_n$ at the nth timestep and $\mathbf{x}_{n+1}$ at the $(n+1)$th timestep makes a velocity contribution of $(\mathbf{x}_{n+1} - \mathbf{x}_n)/\Delta t$ at the point with coordinates $(\mathbf{x}_n + \mathbf{x}_{n+1})/2$. This data can then be appropriately binned to create a velocity profile; we considered bins of size d in the x direction, and created velocity profiles for different vertical slices $|z - z_s| < d/2$.

Since the SFR makes predictions about the velocity profile during steady flow, we choose a time interval $t_1 < t < t_2$ over which the velocity field is approximately constant. Choosing this interval requires some care, since if t_1 is too small then initial transients in the velocity profile can have an effect, and if t_2 is too large, then the free surface can have an influence. For the results reported here, we chose $t_1 = 120\tau$ and $t_2 = 200\tau$.

Figure 6-3 compares the SFR predictions for this environment to the DEM simulation. The displayed simulation data uses a particle contact friction of $\mu_c = 0.3$. Since the typical range of L_s from velocity correlations in simulations [112] and exper-

iments [65] is $3d$ to $5d$, we choose $L_s = 4d$ to generate the approximate SFR solution. We emphasize that this parameter is not fitted. In this geometry, the slip-lines are symmetric about the drift direction causing both $\mathbf{D}_1$ and D_2 to become independent of the internal friction. In prior simulations we have found that particle contact friction has some effect on the flow [113], and analogously the internal friction should play some role in the determination of b. Here, the loss of friction dependence comes from our simplification that $\mathbf{D}_2$ is isotropic. A less simple but more precise definition for $\mathbf{D}_2$ would anisotropically skew the spot diffusion tensor as a function of internal friction: the slip-lines, which we model as the directions along which a spot can move (roughly), intersect at a wider angle as internal friction is increased.

Even so, our simple model captures many of the features of the flow and accurately portrays the dominant behavior. The downward velocity, especially at $z = 10d$, strongly matches the predicted Gaussian. Perhaps a more global demonstration of the underlying stochastic behavior in the SFR is evident in Figure 6-4, where a linear relationship can be seen between the mean square width of v_z and the height, indicating that the system variables are undergoing a type of diffusive scaling. The SFR solution also predicts this linear relationship and, in particular, that the slope should equal $2b = L_s$. The agreement shown in Figure 6-4 for such a typical L_s value is a strong indicator that the role of the correlation length in the flow has been properly accounted for in the SFR.

6.5.2 The Couette geometry

For the Couette geometry, we considered five different interparticle friction coefficients, $\mu_c = 0.1, 0.3, 0.5, 0.7, 0.9$, and for each value an initial packing was generated using a process similar to that for the silo. We consider a large cylindrical container with a side wall at $r = 64d$ with friction coefficient $\mu_w = \mu_c$, and a base at $z = 0$ with friction coefficient $\mu_w = 0$. For each simulation, 160,000 particles are poured in from a height of $z = 48d$ at a rate of $4,848\tau^{-1}$. After all particles are introduced at $t = 33\tau$, the simulation is run for an additional time period of 322τ to allow the particles to settle. After this process has taken place, the initial packings are approx-

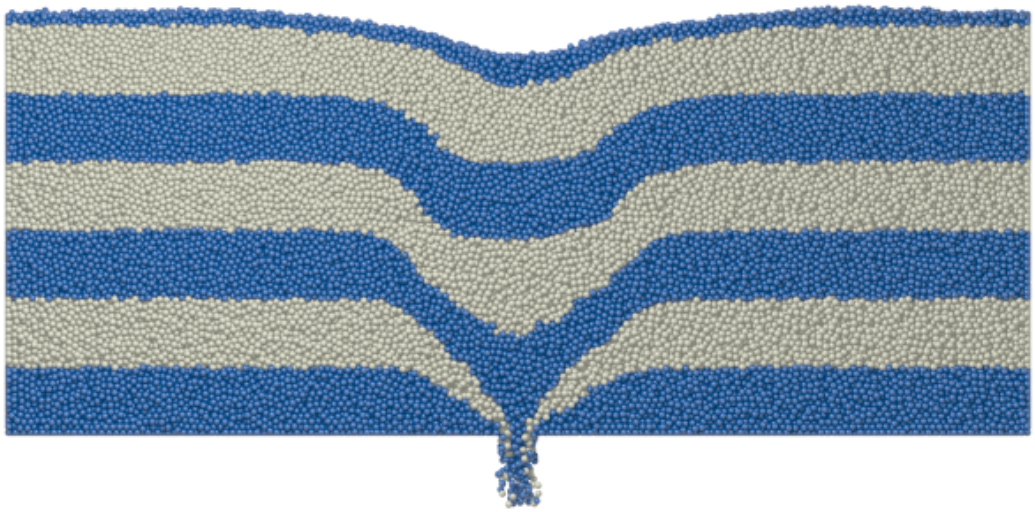

Figure 6-2: A typical snapshot of the silo system during drainage, taken at $t = 60\tau$. The colored bands are initially spaced $10d$ apart, and highlight the deformations that occur during flow.

imately $11.5d$ thick. Packings with $\mu_c = 0.9$ are approximately 2% thicker than those with $\mu_c = 0.1$.

The shearing simulations take place in an annulus between two radii, r_{in} and r_{out}. A rough outer wall is created by freezing all particles which have $r > r_{\text{out}}$; any forces or torques that these particles experience are zeroed during each integration step. Similarly, all particles between $r_{\text{in}} - 4d$ and r_{in} are forced to rotate with a constant angular velocity ω around $r = 0$. Particles with $r < r_{\text{in}} - 4d$ are deleted from the simulation and an extra cylindrical wall with friction coefficient $\mu_w = \mu_c$ is introduced at $r = r_{\text{in}} - 4d$ to prevent stray surface particles from falling out of the shearing region. A typical run is shown in Figure 6-5.

These simulations of the Couette geometry caused some problems with finding an efficient load-balancing scheme for the parallelization. In the silo geometries considered in this thesis, the particles are usually equally distributed in a box-shaped region of space, so when the simulation is divided into a rectangular grid of subdomains, each processor gets approximately the same number of particles, leading to good load-balancing. However, if an annular geometry is subdivided into rectangular grid of subdomains, some the processors may have many more particles than others,

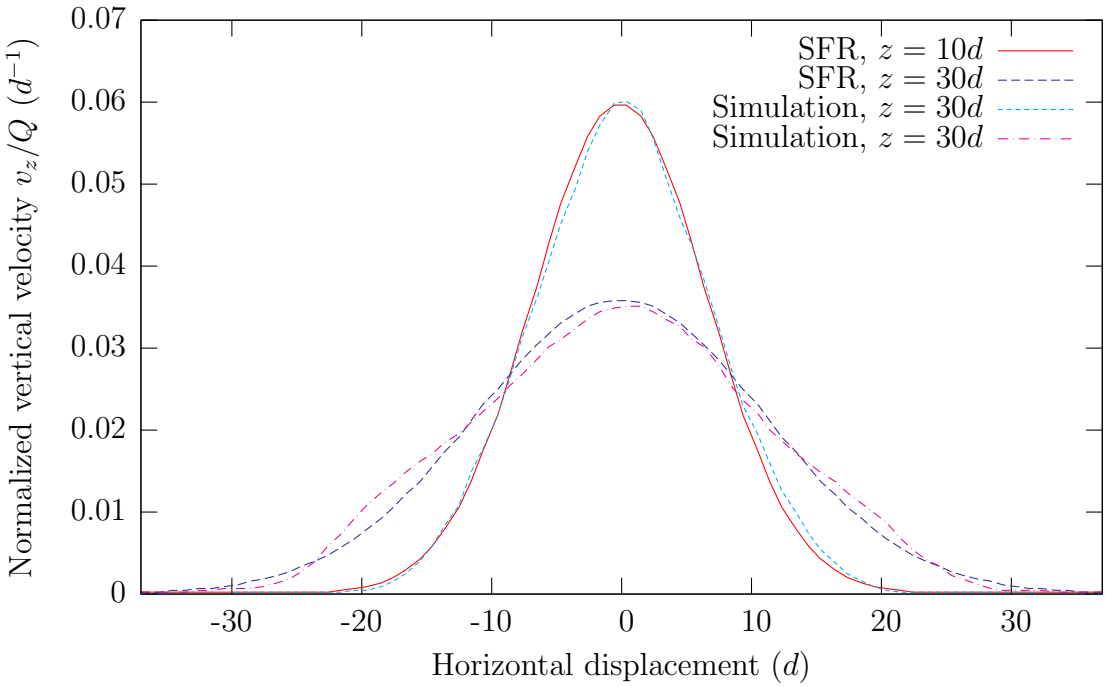

Figure 6-3: Mean downward velocity profiles at two different heights in a wide silo. DEM results are plotted against the SFR predictions at heights of $z = 10d, 30d$.

and since the speed of the code is determined by the speed of the slowest node, this is undesirable. We therefore exploited the radial symmetry of the geometry, and made a 2×2 grid of processors with boundaries at $x = y = 0$, so that each computational subdomain contains approximately a quarter of the total particles. The twenty nodes of the AMCL were then utilised by running five different simulations concurrently.

From the five initial packings, we carried out eight different shear cell simulations to investigate the effects of friction, angular velocity, and inner wall radius. To investigate the effect of friction, five runs were carried out with $\omega = 0.01\tau^{-1}$ and $r_{\text{in}} = 40d$, for $\mu_c = 0.1, 0.3, 0.5, 0.7, 0.9$. To examine the effect of the inner wall radius, an additional run with $r_{\text{in}} = 30d$ and $r_{\text{out}} = 50d$ was carried out, with $\mu_c = 0.3$ and $\omega = 0.01\tau^{-1}$ kept constant. To look at the effect of angular velocity, a further two runs with $\omega = 0.05\tau^{-1}$ and $\omega = 0.2\tau^{-1}$ were carried out, with $\mu_c = 0.5$ and $r_{\text{in}} = 40d$ kept constant. For each simulation, we collected 561 snapshots. For the runs where

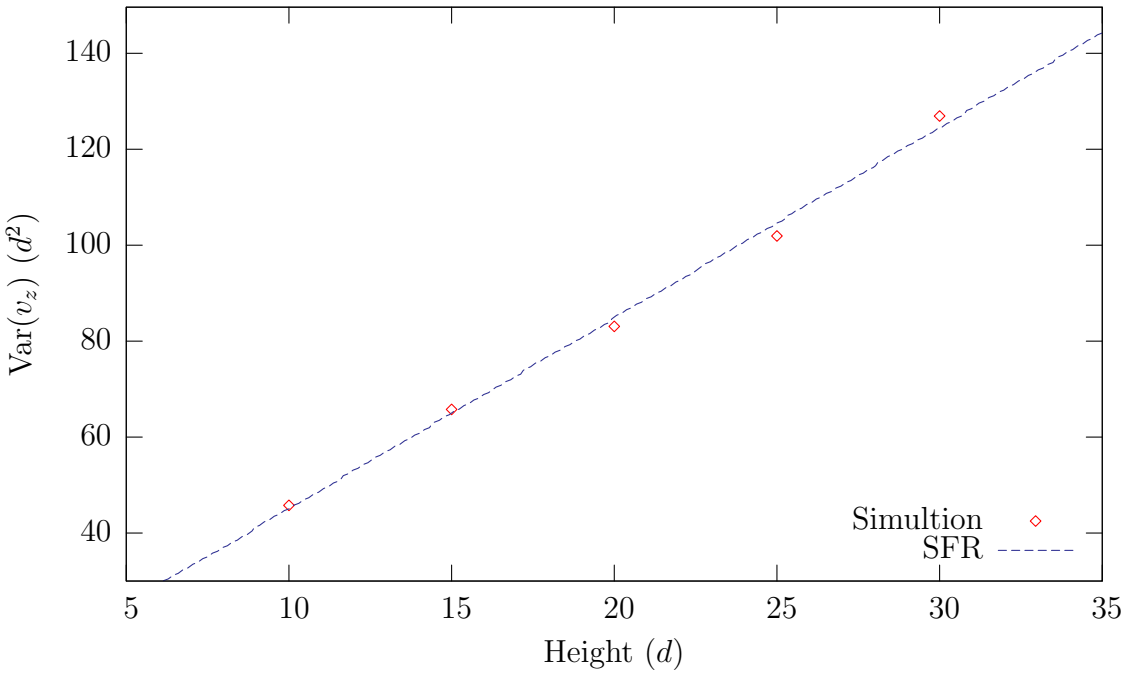

Figure 6-4: Mean square width of the downward velocity across horizontal cross-sections in the DEM simulation, compared to SFR predictions.

$r_{\text{in}} = 40d$, approximately $108,350$ particles were simulated, corresponding to 2.0Gb of data. For the run with $r_{\text{in}} = 30d$, $88,657$ particles were simulated, corresponding to 1.7Gb of data.

The simulation results show a good empirical agreement with previous experimental work on shear cells [80, 87, 72, 21, 88]. In all cases, we see an angular velocity profile that falls off exponentially from the inner cylinder, with a half-width on the order of several particle diameters. Near the inner wall, the flow deviates from exponential, which is an effect seen in some prior studies but is more dramatic here. Following methods similar to those used in silo simulation, we used the snapshots to construct an angular velocity profile. We used bins of size $d/2$ in the radial direction, and we looked at velocity profiles in different vertical slices $z_{\text{low}} < z < z_{\text{high}}$.

Since the simulation geometry is rotationally symmetric, our angular velocity profile can most generally be a function of r, z and t. Ideally, we hope that ω is

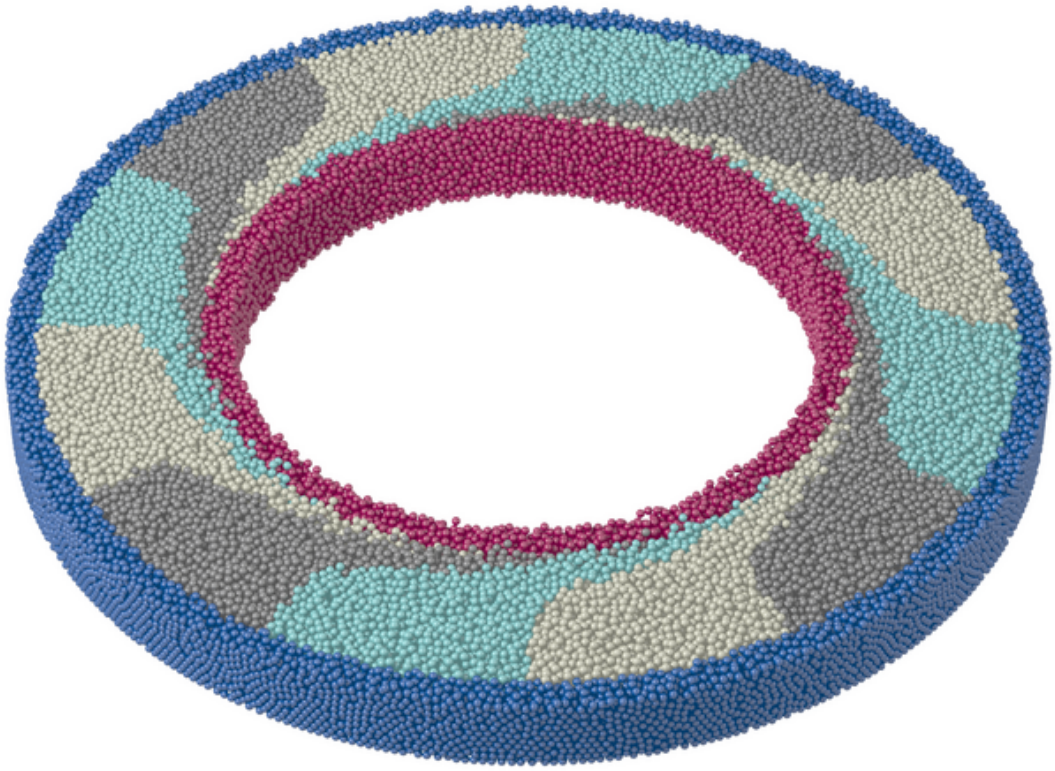

Figure 6-5: A typical snapshot of the annular Couette cell during shearing based on the simulation with $r_{\text{in}} = 40d$, $\omega = 0.01\tau^{-1}$, and $\mu_c = 0.5$. Dark blue particles (with $r > r_{\text{out}}$) are frozen during the simulation, while dark red particles (with $r < r_{\text{in}}$) are rotated with angular velocity ω. The particles between r_{in} and r_{out} undergo shearing. The colored bands of grey, cream, and cyan were initially radial, and in this snapshot, after fifty frames, the deformations can be clearly seen.

primarily a function of r, with only a very weak dependence on z and t, but we began by studying the effects of these other variables. To determine the dependence on time, the velocity profiles were calculated over many different time intervals. As would be expected, the simulation had to be run for small amount of time before the velocity profile would form; this happens on a time scale of roughly 50τ, and the results suggest a longer time is needed for the cases with low friction. However, the data also shows time-dependent effect happening on a longer scale: as the shearing takes place, there is a small but consistent migration of particles away from the rotating wall, which has a small effect on the velocity profile. This effect does eventually appear to saturate, but because of this, we chose to discard the simulation data for $t < 500\tau$ and calculate velocity profiles based on the time window $500\tau < t < 1100\tau$.

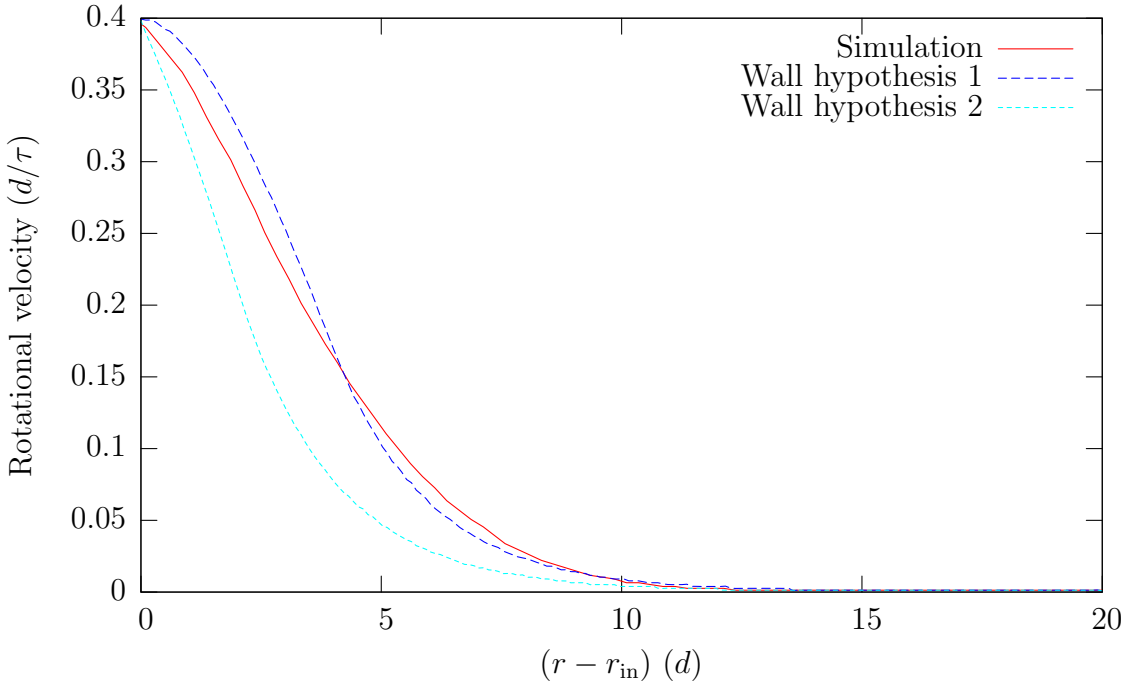

Figure 6-6: SFR solutions for the two different wall hypotheses in the annular Couette geometry ($r_{\text{in}} = 40d, r_{\text{out}} = 60d$) are compared to the simulation results. Both use the same parameters that were used in the silo geometry ($L_s = 4d, \mu_c = 0.3$) and the bead internal friction angle is set at the typical value 25°.

To investigate the angular velocity dependence on the height, we calculated the velocity profiles in five different slices $z_h < z < z_h + d$ for $z_h = d, 3d, 5d, 7d, 9d$. Near the inner rotating wall, the velocity profiles show very little dependence on height. However, in the slow-moving region close to the fixed outer wall, large differences can be seen, with particles in the lowest slice moving approximately 30% slower than those in the central slice, and those in the top slice moving approximate 30% faster. The three central slices show differences of at most 10%, and we therefore chose to use the range $3d < z < 8d$.

The SFR treats the correlation length as a material property independent of the flow geometry or other state variables. To see how well this notion is upheld, we solve the SFR in the annular Couette geometry using the same correlation length ($L_s = 4d$) that was used in the displayed silo prediction, figure 6-4. It is then compared to a simulation of annular flow which uses the same grain properties ($\mu_c = 0.3$).

Results from Figure 6-6 show that regardless of the wall hypothesis, the SFR prediction captures the same qualitative features of the simulation. The SFR and simulation both predict a flatter range near the inner wall, followed by exponential decay. Near the inner wall, it does appear that wall hypothesis 1 ("no slip condition" for spots) gives a closer match to the simulation.

The SFR, when applied to the annular flow geometry, does predict a slight dependence of the flow on the internal friction. We emphasize that internal friction is not the same quantity as particle contact friction μ_c, though we believe if the contact friction is increased, inevitably, the internal friction must be as well. Spherical grains almost always have internal friction angles in the range $\phi = 20^\circ$ to $\phi = 30^\circ$, so to represent this range as best as possible, we simulated flows varying the particle contact friction from $\mu_c = 0.1$ to $\mu_c = 0.9$. Figure 6-7 displays velocity profiles for five different values of friction. In the semi-log format, profiles appear almost linear over the range $45d < r < 58d$ indicating a very good fit to an exponential model of velocity.

Since the curves in the figure are very close, and exhibit some experimental noise, it is difficult to discern any small differences in the widths of the velocity profiles.

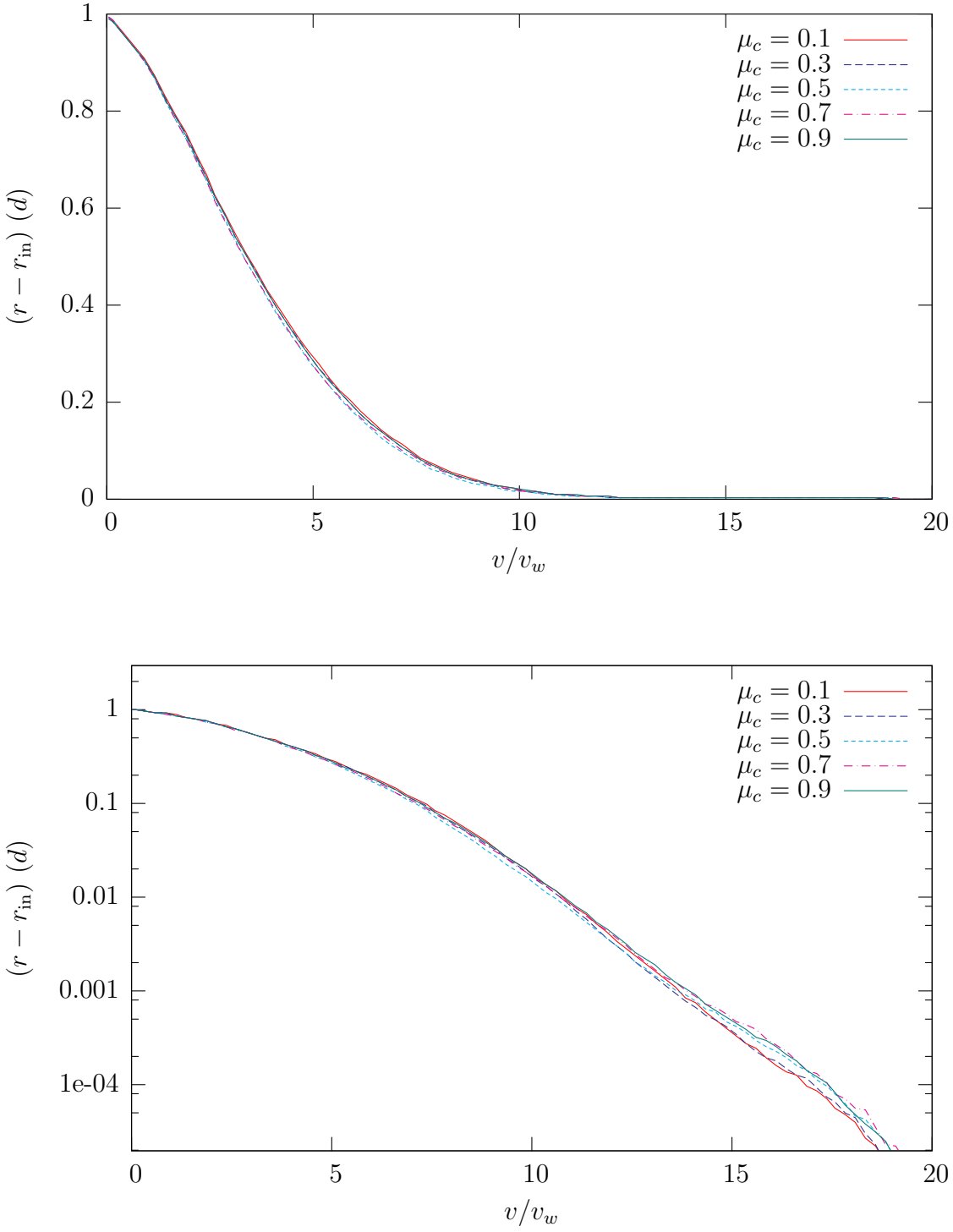

Figure 6-7: Velocity profiles for five different values of μ_c, where $r_{\text{in}} = 40d$ and $\omega = 0.01\tau^{-1}$, plotted on a linear scale (top) and on a semi-logarithmic scale (bottom).

μ_c	b
0.1	$0.974d$
0.3	$0.983d$
0.5	$1.033d$
0.7	$1.046d$
0.9	$1.032d$

ϕ	b
20°	$1.026d$
22°	$1.038d$
24°	$1.052d$
26°	$1.069d$
28°	$1.084d$
30°	$1.102d$

Table 6.1: (Left) Simulation: Half-widths of the shearing velocity profiles for different values of μ_c, calculated by fitting the functional form $f(r) = a - (\log 2)r/b$ to $\log v/v_w$ over the range $45d < r < 58d$. (Right) SFR: Fits the predictions to the same form and uses $L_s = 3d$.

However, table 6.1 shows the results of applying linear regression to extract a half-width for each velocity profile. We see differences on the order of 5%, roughly in line with the SFR. More importantly, the trend of increasing flow width with increasing friction is seen in both.

When the inner wall radius is decreased, Figure 6-8 indicates that the shear band shrinks but the decay behavior in the tail changes only minimally. The SFR predicts this qualitative trend as well, but significantly underestimates the size of the shear-band decrease.

In agreement with past work on Couette flow [80, 21], we too find that the normalized flow profile is roughly unaffected by the shearing rate (see Figure 6-9). As previously discussed, this behavior is in agreement with the SFR, which always permits flow fields to be multiplied by a constant.

6.6 Conclusion

The crucial principles motivating the Stochastic Flow Rule have been presented, and its validity has been assessed by checking analytical predictions for silo and annular Couette flow against discrete-element simulations. Using the same parameters for both cases, without any fitting, the SFR manages good predictions for these two very different flow geometries, which it seems cannot be described, even qualitatively, by any other model. The model was also shown to capture the "diffusive" type flow

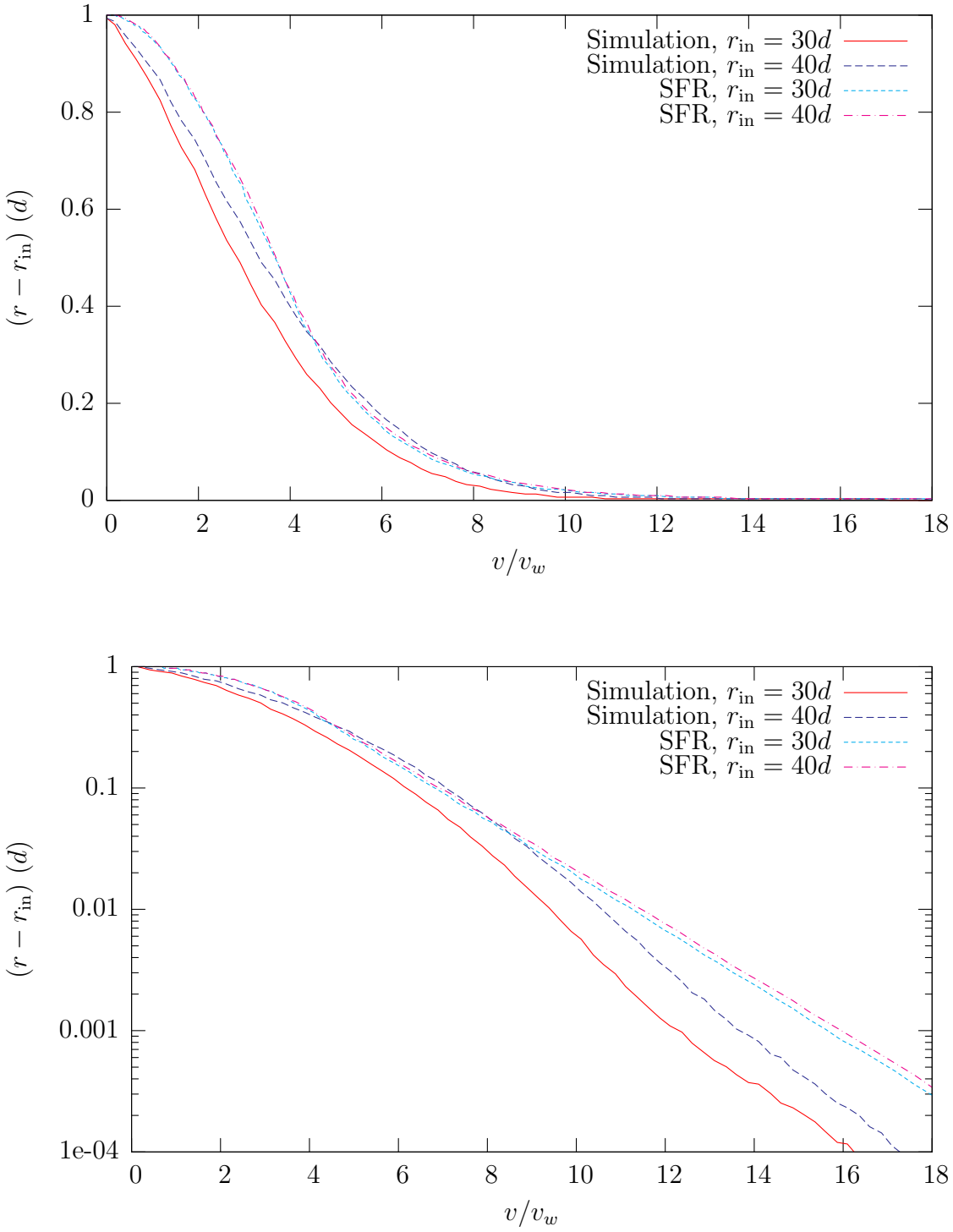

Figure 6-8: DEM simulation results for the flow profile compared to SFR predictions, for two different values of r_{in}. For solidarity with the silo flow predictions, the SFR solutions use $L_s = 4d$.

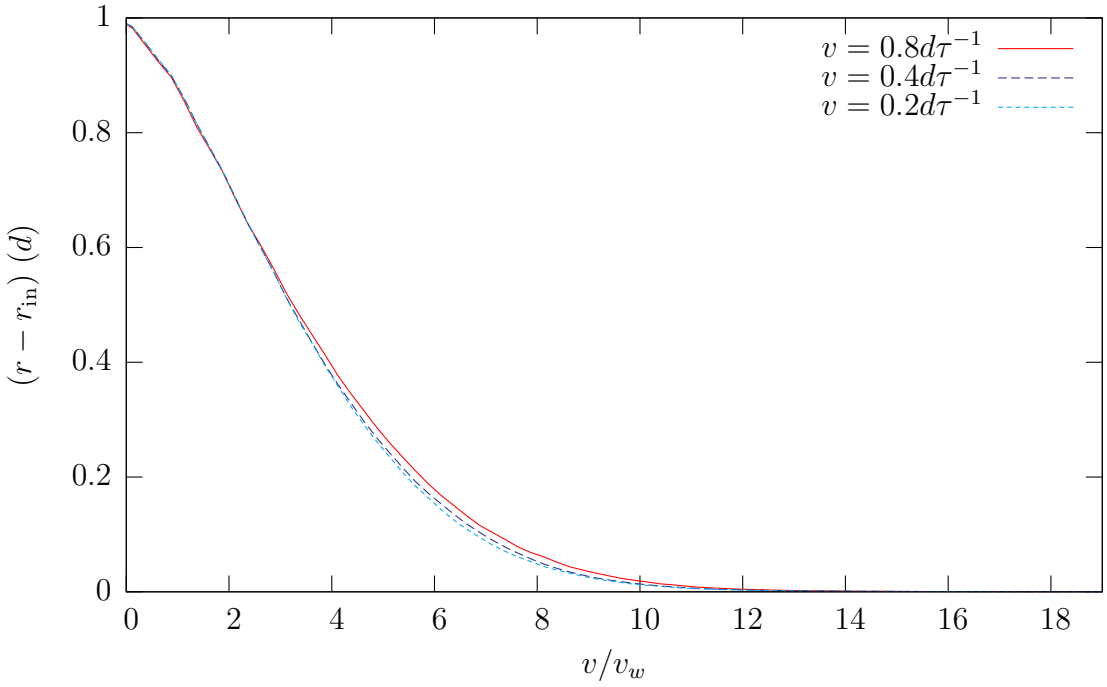

Figure 6-9: Velocity profiles for three different angular velocities, with $\mu_c = 0.5$ and $r_{\text{in}} = 40d$. The time windows over which the velocities are computed are scaled according to the angular velocity.

properties unique to granular materials such as Gaussian downward velocity in the draining silo and exponentially decaying velocity in the annular Couette cell.

Our simulations also indicate that the slight changes in flow brought on by varying the inter-particle contact friction in the annular flow geometry match the trends the SFR predicts when the internal friction angle is appropriately varied. The trend is also captured when the inner wall radius is varied, though the quantitative agreement is not as strong. In agreement with past studies on annular Couette flow, and in validation of one of the first principles behind the SFR, we find in our simulations that the flow rate does not significantly affect the normalized flow profile over a significant range of rates.